Supporting information

Zero-valent iron/biochar hybrid rewires microbial electron transfer and energetics for upgrading waste activated sludge to medium-chain fatty acids

Additional experimental details

Text 1. The synthesis and characterization of ZVI/BC

Biochar was produced through pyrolysis of rice stalk at 500°C in oxygen-limited conditions, following the procedure provided by Lou et al. (2024). The produced biochar was crushed and sieved to ensure its particle size was lower than 150 μm and then used to synthesize the ZVI/BC composite. The ZVI/BC was synthesized through the chemical reduction method described by previous studies (Qian et al., 2017; Ahmad et al., 2022). First, biochar and ferrous sulfate ($FeSO_4 \cdot 7H_2O$) with a mass ratio of biochar/Fe=5 (Li et al., 2023) were dissolved in 250 mL of deionized water with pH 4.0, agitating on a shaker at 150 rpm and 25 °C for 24 h. Then, the solution was moved into a three-neck flask with 50 mL of ethanol, and the dissolved O_2 in the solution was excluded by purging N_2 for 1 h under strong stirring. Subsequently, 200 mL $NaBH_4$ solution was added dropwise under vigorous stirring and continuous N_2 purging, the whole reaction lasted for 2 h. When the reaction came to an end, products were separated from the solution with a magnet. After being washed with ethanol, the products were finally vacuum-dried and preserved in a sealed container for subsequent characterization and addition.

A scanning electron microscopy (SEM; JSM7900F, Japan) equipped with an energy-dispersive X-ray spectroscopy (EDS) system was used to characterize the surface morphology of ZVI/BC. X-ray diffraction (XRD) was further applied to determine its crystalline structure in the range of 10°-90° with a scan rate of 2°/min The chemical states of the surface elements of ZVI/BC were determined by X-ray photoelectron spectroscopy (XPS; ESCALAB 250Xi, America). All the binding energies were calibrated and referenced to the C1s peak at 284.8 eV.

Text 2. Extraction protocol of EPS

In this study, three fractions of EPS were extracted according to the protocol provided by Cai et al. (2018) and Cheng et al. (2024). First, 30 mL of sludge samples were centrifuged at 3000 ×g and 4 °C for 15 min to collect the supernatant fluids containing S-EPS. Then, solids at the bottom of the centrifuge tubes were re-suspended to the original volume by adding 0.05% (w/w) NaCl solution pre-heated to 70 °C, vortexed and incubated for 1 min at 50 °C. The suspension was then immediately centrifuged at 4000g and 4 °C for 10 min to obtain the supernatant fluids containing LB-EPS. Finally, after recovering the original volume with 0.05% NaCl solution, samples were sonicated (20 kHz) for 5 min, thermally treated at 60 °C for 30 min, and centrifuged at 8000 ×g for 20 min (4 °C) to collect supernatant liquids as TB-EPS. All EPS samples were filtered through a 0.45 μm membrane filter and stored at 4 °C before analysis.

Text 3. FRI analysis

The Raman and Rayleigh scattering on 3D-EEM spectra was deducted by using MATLAB software. Then, the fluorescence region integration (FRI) analysis was conducted to evaluate the relative content of substances corresponding to each region (Liu et al., 2024). The calculation formulas are shown in Eq. (1) to Eq. (3).

$$\Phi_{i,n}=MF_i \iint_{ex\,em} I(\lambda_{ex}\lambda_{em})\,d\lambda_{ex}\,d\lambda_{em} \quad (1)$$

$$\Phi_{T,n}=\sum_{i=1}^{5}\Phi_{i,n} \quad (2)$$

$$P_{i,n}=\frac{\Phi_{i,n}}{\Phi_{T,n}}\times 100\% \quad (3)$$

Detailly, $\Phi_{i,n}$ represents the integral standard volume of fluorescence region i; MF_i represents the multiplication factor; λ_{em} and λ_{ex} represent the emission and excitation wavelengths, respectively. $I(\lambda_{ex}\lambda_{em})$ represents the fluorescence intensity corresponding to the excitation/emission wavelengths; $\Phi_{T,n}$ represents the total fluorescence area integral standard volume; $P_{i,n}$ represents the ratio of the integral standard volume of fluorescence region i to the integral standard volume of the total fluorescence region.

Text 4. Calculation of electron transfer capacity (ETC), electron acceptor capacity (EAC), and electron donor capacity (EDC)

The CV analysis was performed with the scanning voltage of -1.6V~1.2V (vs. Ag/AgCl) and the scan rate of 60 mV/s. Previous studies figured the number of transferred electrons can be quantified by integrating the current-time curve from the CV voltammogram, and the ETC, EAC, and EDC can be calculated according to the following equations (Yuan et al., 2012).

$$ETC = \frac{\int (I_{red} + I_{ox})dt}{F \cdot VS}$$

$$EAC = \frac{\int I_{red}dt}{F \cdot VS}$$

$$EDC = \frac{\int I_{ox}dt}{F \cdot VS}$$

Where, I_{red} (A) and I_{ox} (A) refer to the reductive and oxidative currents; F equals 964853.33 C/mol e^-; VS (g) refers the mass of volatile solids in the measured sludge samples.

Text 5. High-throughput sequencing and microbial data analyses

The microbial samples were collected at the end of fermentation. According to previous studies (Yin and Wang, 2021), primers 515F and 806R were selected to conduct PCR amplification, and V4-V5 region was amplified. The working volume of PCR reaction mixture was 20 μL, which contains template DNA (10 ng), 5 × FastPfu Buffer (4 μL), 2.5 mM dNTPs (2 μL), two primers (each with 0.8 μL), and FastPfu Polymerase (0.4 μL). The specific PCR conditions were set as follows (Yin and Wang, 2016): 95 °C for 2 min, 95 °C for 30 s repeated 25 cycles, 55 °C for 30 s, 72 °C for 30 s and a final extension at 72 °C for 5 min. All the reactions were in triplicate. Following, AxyPrep DNA Gel Extraction Kit was used to purify the obtained PCR product, and the QuantiFluorTM-ST was further applied for PCR products quantification. The amplicon sequencing was conducted on the Illumina MiSeq PE250 platform (Majorbio Bio-pharm Biotechnology, Shanghai, China). QIIME (version 2) was used to quality-filter the raw fastq files. Optional Units (OTUs) with over 97% similarity were clustered.

Based on the data obtained from the microbial analysis, LEfSe analysis was performed by LEfSe software to determine the microorganisms most sensitive to ZVI dosage. The PICRUSt2 analysis was used to understand the impacts of ZVI/BC on MCFAs production from the perspective of microbial metabolism, following the methodology proposed by Langille et al. (2013). The metabolic pathways involved in MCFAs production were constructed according to the KEGG database. All the databases and software used in this study were in their newest version.

Text 6. Modified Gompertz equation

The cumulative MCFAs concentrations were fitted to the modified Gompertz equation using Origin 2024 software, aims at obtaining the kinetic parameters for MCFAs production.

$$H=P_m \cdot \exp\{-\exp[\frac{R_m e}{P_m}(\lambda-t)+1]\}$$

Where H refers the cumulative MCFAs concentration (mg/L); P_m refers the maximum MCFAs concentration potential (mg/L); R_m refers the maximal MCFAs production rate (mg/L/d); λ refers the lag time in MCFAs production (d); t refers the fermentation time (d); and e is a constant value 2.718.

Text 7. Typical CE parameters

Typical CE parameters, including carbon conversion efficiency (CCE), electron transfer efficiency (ETE) of MCFAs, MCFAs selectivity, and ethanol\acetate utilization efficiency, were calculated to evaluate the performance of the CE process. Detailed calculations of these parameters were as follows (Eq. 1-4):

$$\mathrm{CCE} = \frac{\text{Total produced acids and alcohols during CE process}}{\text{Total consumed acids and alcohols during CE process}} \quad (1)$$

$$\text{ETE of MCFAs} = \frac{\text{Electrons of the produced MCFAs}}{\text{Electrons of the consumed substrates}} \quad (2)$$

$$\text{MCFAs selectivity} = \frac{\text{MCFAs produced in CE}}{\text{The acids and alcohols produced in CE}} \quad (3)$$

$$\text{Ethanol\acetate utilization efficiency} = \frac{\text{Consumed ethanol\acetate in CE}}{\text{Original concentration at initial CE}} \quad (4)$$

The carbons (mmol C/L) contained in each substance (mmol/L) and the electrons (mmol e^{-1}/mmol) consumed for its production were listed as follows: 1 acetate equals 2 C and 8 e^{-1}, 1 ethanol equals 2 C and 12 e^{-1}, 1 propionate equals 3 C and 14 e^{-1}, 1 butyrate equals 4 C and 20 e^{-1}, 1 butyrate equals 4 C and 20 e^{-}, 1 butanol equals 4 C and 24 e^{-}, 1 valerate equals 5 C and 26 e^{-}, 1 caproate equals 6 C and 32 e^{-}, 1 hexanol equals 6 C and 36 e^{-}, 1 heptylate equals 7 C and 38 e^{-}, 1 caprylate equals 8 C and 44 e^{-}.

Text 8. GC parameters

Concentrations of carboxylates and alcohols in liquid phase were determined by a gas chromatograph (HP 7890, Agilent, USA), equipped with a flame ionization detector and a DB-FFAP column (60 m × 0.32 mm × 0.25 μm). The column flow was 2.2 mL/min (He). The injected sample volume was 0.8 uL. The inlet temperature was 160 ℃, with a split ratio of 15:1. The oven temperature was kept at 80 ℃ for 1 min, and then increased to 230 ℃ at the rate of 15 ℃/min. The detector temperature was set to be 250 ℃. All the parameters in liquid phase were measured after filtering through a 0.45 um filter.

Text 9. Comparison of ZVI/BC with individual ZVI and BC treatments

A parallel comparison experiment was conducted to evaluate the performance of ZVI/BC relative to its individual components. Four treatments were included: control, ZVI, BC, and ZVI/BC. All materials were added before the acidification stage, and the remaining fermentation conditions were consistent with those used in the main experiment.

During acidification, acetate and butyrate were the dominant products (Supplementary Fig. 5). By day 12, the total concentration of detected acids and alcohols reached approximately 3.4 g COD/L in the ZVI/BC group, compared with 3.3, 3.2, and 3.0 g COD/L in the BC, ZVI, and control groups, respectively. These results indicate that ZVI/BC produced a modest improvement in precursor accumulation during acidification.

The difference among the treatments became more pronounced during chain elongation (Supplementary Fig. 6). By day 46, caproate concentrations reached approximately 10.0, 7.5, 7.1, and 5.9 g COD/L in the ZVI/BC, BC, ZVI, and control groups, respectively. Thus, caproate accumulation in the ZVI/BC group was 33.3% higher than that in the BC group, 40.8% higher than that in the ZVI group, and 69.5% higher than that in the control. The higher caproate concentration was also accompanied by greater conversion of the residual butyrate pool. Overall, the ZVI/BC composite showed higher chain-elongation performance than either ZVI or BC alone under the tested conditions.

Figures

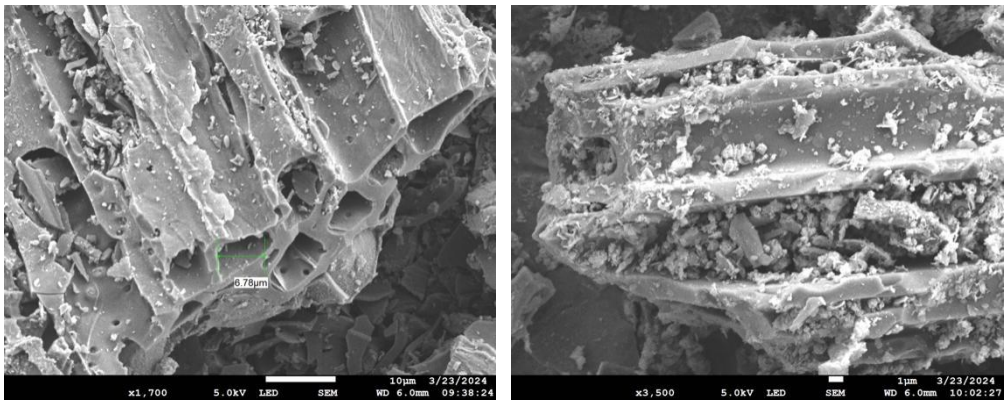

Figs. 1. The scanning electron microscope (SEM) spectra of synthesized ZVI/BC

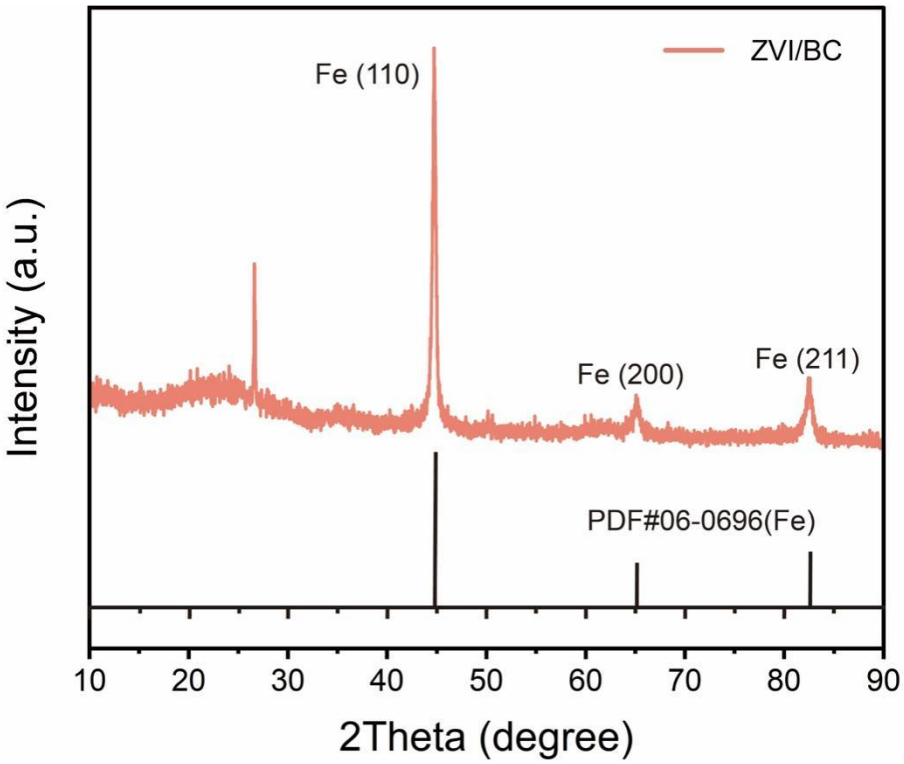

Figs. 2. XRD spectrum of the synthesized ZVI/BC composite

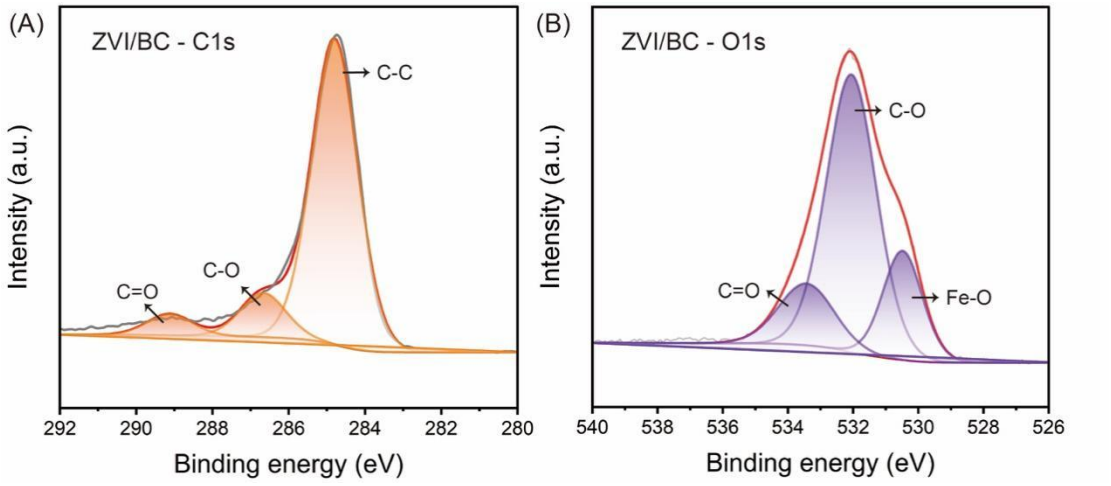

Figs. 3. The (A) C1s and (B) O1s XPS spectra of synthesized ZVI/BC

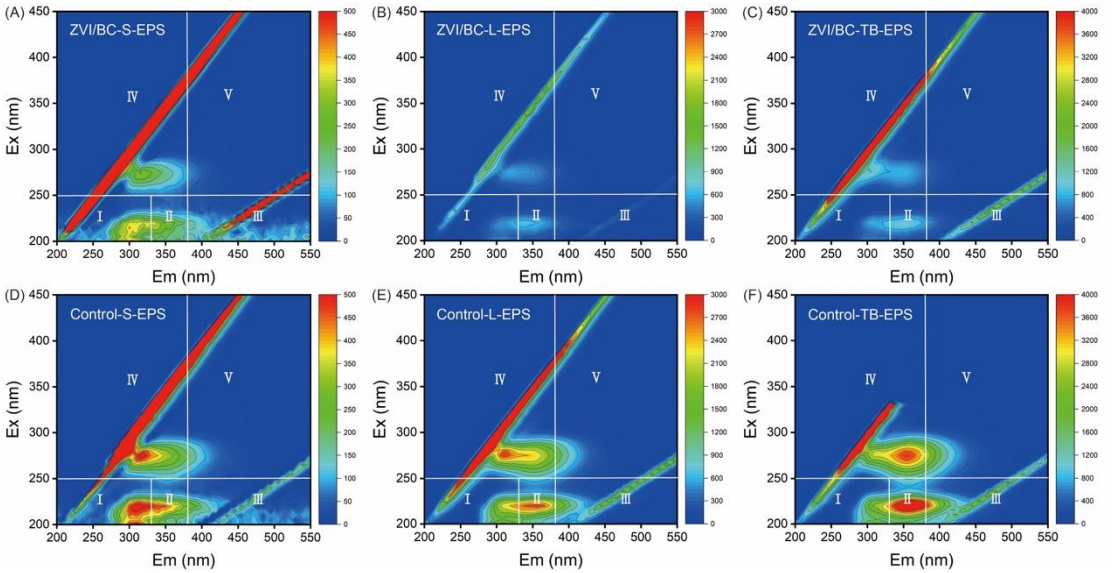

Figs. 4. 3D-EEM spectra of different fractions of EPS in the control and ZVI/BC sludge samples at the end of fermentation (S-EPS were diluted 250 times, L-EPS were diluted 50 times, and TB-EPS were diluted 10 times before measurement).

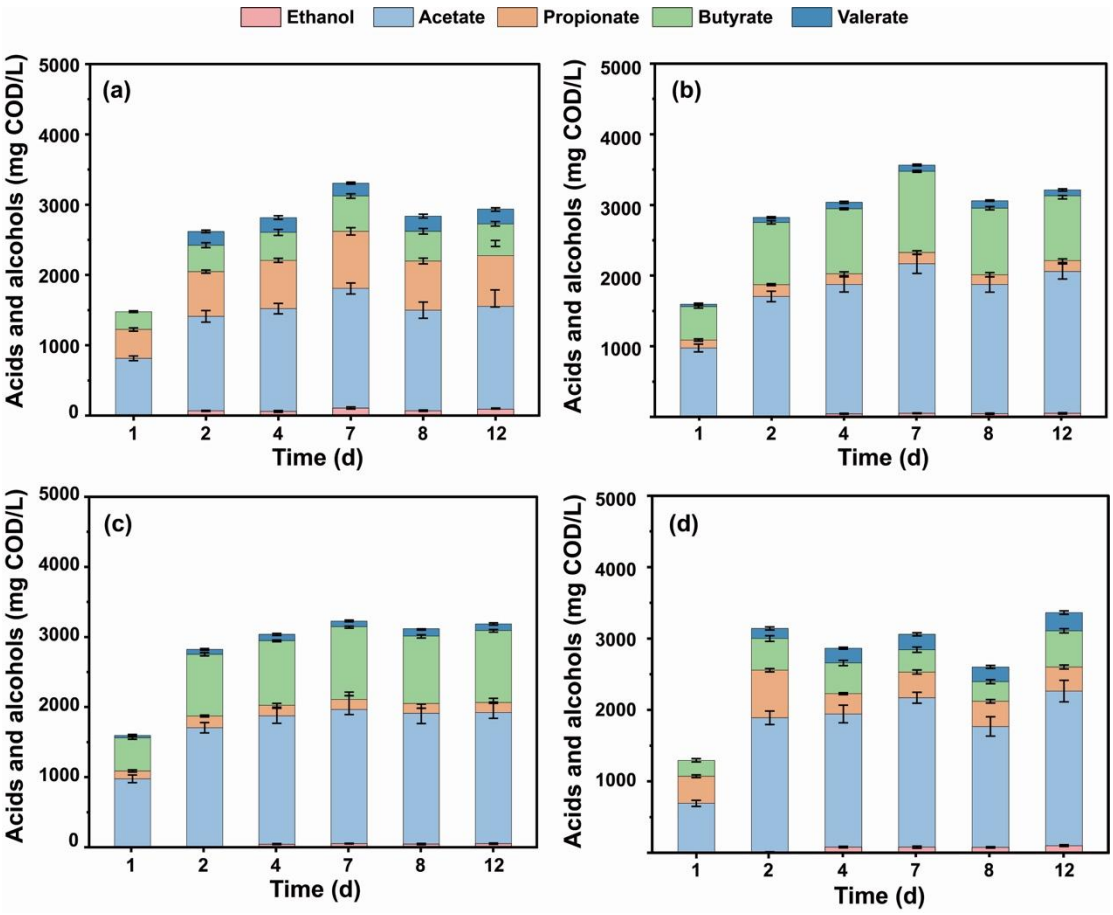

Figs. 5. Concentrations of acids and alcohols during the acidification stage in the (A) control, (B) BC, (C) ZVI, and (D) ZVI/BC groups.

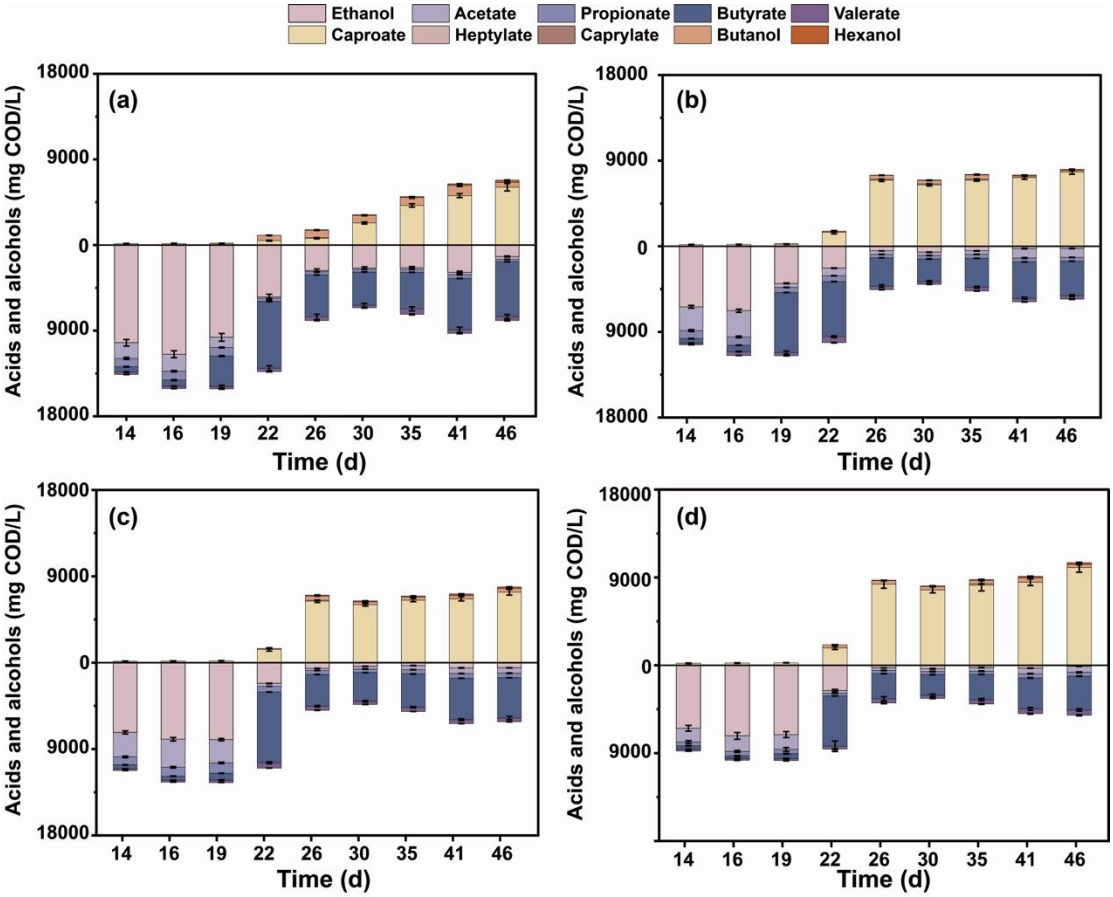

Figs. 6. Substrate and product concentrations during the chain elongation stage in the (A) control, (B) BC, (C) ZVI, and (D) ZVI/BC groups. Ethanol and short-chain fatty acids, including acetate, propionate, butyrate, and valerate, are shown below the horizontal line as substrates. Medium-chain fatty acids and long-chain alcohols are shown above the horizontal line as products.

Tables

Table 1 Kinetic analysis for MCFAs production during the CE process.

Group	P (mg/L)	λ (d)	R_{max} (mg/L/d)	R^2
Control	2371.2	6.3	772.3	0.999
ZVI/BC	4456.9	7.2	2505.0	0.999

Table 2 The relative abundances of key modules involved in electron transport

	Module	Enzyme Description	Control	ZVI/BC
Complex I	M00143	NADH dehydrogenase (ubiquinone) Fe-S protein/flavoprotein complex, mitochondria	4.93E-06	2.09E-05
	M00144	NADH:quinone oxidoreductase, prokaryotes	1.784	1.739
	M00145	NAD(P)H:quinone oxidoreductase (cyanobacteria)	0.015	0.014
	M00146	NADH dehydrogenase (ubiquinone) 1 alpha subcomplex	2.46E-05	1.05E-05
Complex II	M00149	Succinate dehydrogenase, prokaryotes	0.307	0.270
	M00150	Fumarate reductase, prokaryotes	0.025	0.022
Complex III	M00151	Cytochrome bc1 complex respiratory unit	0.164	0.149
	M00152	Cytochrome bc1 complex	0.059	0.037
Complex IV	M00154	Cytochrome c oxidase	0.096	0.082
	M00155	Cytochrome c oxidase, prokaryotes	0.366	0.337
	M00156	Cytochrome c oxidase, cbb3-type	0.082	0.044
	M00416	Cytochrome aa3-600 menaquinol oxidase	0.001	0.001
	M00417	Cytochrome o ubiquinol oxidase	0.043	0.041
Complex V	M00157	F-type ATPase, prokaryotes & chloroplasts	1.266	1.338
	M00159	V/A-type ATPase, prokaryotes	0.329	0.276
Glycolysis	M00001	Glycolysis (Embden-Meyerhof pathway), glucose => pyruvate	2.451	2.507
	M00002	Glycolysis, core module involving three-carbon compounds	1.545	1.601
	M00003	Gluconeogenesis, oxaloacetate => fructose-6P	1.830	1.900
	M00004	Pentose phosphate pathway (Pentose phosphate cycle)	1.380	1.402
	M00005	PRPP biosynthesis, ribose 5P => PRPP	0.188	0.199
TCA cycle	M00009	Citrate cycle (TCA cycle, Krebs cycle)	2.320	2.360

	M00011	Citrate cycle, second carbon oxidation, 2-oxoglutarate => oxaloacetate	1.900	1.980
	M00579	Phosphate acetyltransferase-acetate kinase pathway, acetyl-CoA => acetate	0.254	0.261
Pyruvate	M00307	Pyruvate oxidation, pyruvate => acetyl-CoA	0.889	0.860
oxidation	M00308	Semi-phosphorylative Entner-Doudoroff pathway, gluconate => glycerate-3P	0.546	0.553
NAD	M00115	NAD biosynthesis, aspartate => NAD	0.707	0.711
Ubiquinone and	M00116	Menaquinone biosynthesis, chorismate => menaquinol	0.511	0.519
menadione	M00117	Ubiquinone biosynthesis, prokaryotes, chorismate => ubiquinone	0.288	0.258
FMN/FAD	M00125	Riboflavin biosynthesis, GTP => riboflavin/FMN/FAD	0.771	0.817

Table 4 The relative abundances of key encoding genes associated with pili and electronic bifurcation

	KO	KO Description	Control	ZVI/BC
	K02650	type IV pilus assembly protein PilA	0.034	0.038
	K02651	pilus assembly protein Flp/PilA	0.021	0.018
	K02652	type IV pilus assembly protein PilB	0.062	0.063
	K02653	type IV pilus assembly protein PilC	0.058	0.057
	K02655	type IV pilus assembly protein PilE	0.004	0.001
	K02656	type IV pilus assembly protein PilF	0.003	0.001
	K02661	type IV pilus assembly protein PilK	4.09E-08	1.06E-05
	K02662	type IV pilus assembly protein PilM	0.036	0.040
Pili	K02663	type IV pilus assembly protein PilN	0.007	0.004
	K02664	type IV pilus assembly protein PilO	0.009	0.008
	K02665	type IV pilus assembly protein PilP	0.003	0.001
	K02666	type IV pilus assembly protein PilQ	0.004	0.002
	K02671	type IV pilus assembly protein PilV	0.003	0.001
	K02672	type IV pilus assembly protein PilW	0.003	0.001
	K02673	type IV pilus assembly protein PilX	0.003	0.000
	K02674	type IV pilus assembly protein PilY1	0.003	0.001
	K02676	type IV pilus assembly protein PilZ	0.003	0.001
	K03521	electron transfer flavoprotein beta subunit	0.107	0.118
EtfAB/bcd	K03522	electron transfer flavoprotein alpha subunit	0.109	0.122
complex	K00313	electron transfer flavoprotein-quinone oxidoreductase [EC:1.5.5.-]	0.005	0.004
	K00248	butyryl-CoA dehydrogenase [EC:1.3.8.1]	0.052	0.054
Rnf	K03612	Na+-translocating ferredoxin:NAD+ oxidoreductase subunit G	0.029	0.031

	K03613	Na+-translocating ferredoxin:NAD+ oxidoreductase subunit E	0.034	0.038
	K03614	Na+-translocating ferredoxin:NAD+ oxidoreductase subunit D [EC:7.2.1.2]	0.036	0.039
	K03615	Na+-translocating ferredoxin:NAD+ oxidoreductase subunit C [EC:7.2.1.2]	0.032	0.034
	K03616	Na+-translocating ferredoxin:NAD+ oxidoreductase subunit B [EC:7.2.1.2]	0.019	0.024
	K03617	Na+-translocating ferredoxin:NAD+ oxidoreductase subunit A	0.033	0.037
	K03388	heterodisulfide reductase subunit A2 [EC:1.8.7.3 1.8.98.4 1.8.98.5 1.8.98.6]	7.20E-04	1.39E-03
$HydA_2B_2C_2$	K03389	heterodisulfide reductase subunit B2 [EC:1.8.7.3 1.8.98.4 1.8.98.5 1.8.98.6]	4.59E-04	7.97E-04
	K03390	heterodisulfide reductase subunit C2 [EC:1.8.7.3 1.8.98.4 1.8.98.5 1.8.98.6]	5.40E-04	7.84E-04

Table 5 The relative abundances of key encoding genes associated with bacterial chemotaxis

	KO	KO Description	Control	ZVI/BC
		MCP		
mcp	K03406	methyl-accepting chemotaxis protein	0.240	0.245
Tsr	K05874	methyl-accepting chemotaxis protein I, serine sensor receptor	0.003	0.001
Tar	K05875	methyl-accepting chemotaxis protein II, aspartate sensor receptor	0.002	0.000
Trg	K05876	methyl-accepting chemotaxis protein III, ribose and galactose sensor receptor	5.66E-05	5.30E-05
Tap	K05877	methyl-accepting chemotaxis protein IV, peptide sensor receptor	2.45E-05	7.42E-06
		Two-component system		
CheZ	K03414	chemotaxis protein CheZ	0.004	0.002
CheR	K00575	chemotaxis protein methyltransferase CheR [EC:2.1.1.80]	0.050	0.047
CheB	K03412	two-component system, chemotaxis family, protein-glutamate methylesterase/glutaminase [EC:3.1.1.61 3.5.1.44]	0.051	0.049
CheA	K03407	two-component system, chemotaxis family, sensor kinase CheA [EC:2.7.13.3]	0.047	0.046
CheY	K03413	two-component system, chemotaxis family, chemotaxis protein CheY	0.060	0.056
		Flagellar switch protein		
FliG	K02410	flagellar motor switch protein FliG	0.041	0.042
FliM	K02416	flagellar motor switch protein FliM	0.044	0.048
FliN	K02417	flagellar motor switch protein FliN/FliY	0.056	0.061
FliJ	K02413	flagellar FliJ protein	0.030	0.036
		Flagellar motor protein		
MotA	K02556	chemotaxis protein MotA	0.052	0.058
MotB	K02557	chemotaxis protein MotB	0.056	0.061

Table 6 Relative abundances of key enzymes involved in CE reactions.

Enzyme No.	Enzyme	Enzyme Description	Control	ZVI/BC
		Acetyl-CoA production		
1	1.1.1.1	Alcohol dehydrogenase	0.302	0.308
2	1.2.1.10	Acetaldehyde dehydrogenase (acetylating)	0.100	0.114
3	1.2.7.4	Carbon-monoxide dehydrogenase (ferredoxin)	0.080	0.108
4	2.1.1.245	Co-methyltransferase	0.063	0.088
		Reverse β oxidation pathway		
5	2.3.1.16	Acetyl-CoA C-acyltransferase	0.081	0.071
6	1.1.1.35	3-hydroxyacyl-CoA dehydrogenase	0.047	0.028
7	4.2.1.17	Enoyl-CoA hydratase	0.306	0.301
		Butyrate metabolism pathway		
8	2.3.1.9	Acetyl-CoA C-acetyltransferase	0.363	0.341
9	5.1.2.3	3-hydroxybutyryl-CoA epimerase	0.018	0.014
	1.1.1.363	Glucose-6-phosphate dehydrogenase (NAD(P)(+))	0.074	0.068
	1.1.1.35	3-hydroxyacyl-CoA dehydrogenase	0.047	0.028
	1.1.1.157	3-hydroxybutyryl-CoA dehydrogenase	0.128	0.122
	4.2.1.17	Enoyl-CoA hydratase	0.306	0.301
10	4.2.1.55	3-hydroxybutyryl-CoA dehydratase	0.012	0.009
	1.3.1.86	Crotonyl-CoA reductase	0.024	0.030
12	2.8.3.8	Acetate CoA-transferase	0.059	0.066
		Fatty acid biosynthesis pathway		
13	6.4.1.2	Acetyl-CoA carboxylase	0.345	0.336

14	2.3.1.39	[Acyl-carrier-protein] S-malonyltransferase	0.127	0.125
15	2.3.1.179	Beta-ketoacyl-[acyl-carrier-protein] synthase II	0.153	0.140
	2.3.1.180	Beta-ketoacyl-[acyl-carrier-protein] synthase III	0.158	0.156
16	1.1.1.100	3-oxoacyl-[acyl-carrier-protein] reductase	0.493	0.467
17	4.2.1.59	3-hydroxyacyl-[acyl-carrier-protein] dehydratase	0.115	0.105
18	1.3.1.9	Enoyl-[acyl-carrier-protein] reductase	0.146	0.144
		Final CE step		
19	3.1.2.23	4-hydroxybenzoyl-CoA thioesterase	0.005	0.004
	3.1.2.29	Fluoroacetyl-CoA thioesterase	0.001	0.001
	3.1.2.30	(3S)-malyl-CoA thioesterase	0.002	0.001

References

Ahmad S, Liu X, Tang J, Zhang S (2022). Biochar-supported nanosized zero-valent iron (nZVI/BC) composites for removal of nitro and chlorinated contaminants. Chemical Engineering Journal, 431: 133187

Cai M Q, Hu J Q, Wells G, Seo Y, Spinney R, Ho S H, Dionysiou D D, Su J, Xiao R, Wei Z (2018). Understanding mechanisms of synergy between acidification and ultrasound treatments for activated sludge dewatering: From bench to pilot-scale investigation. Environmental Science & Technology, 52(7): 4313−4323

Cheng Y, Lu C, Gao S, Koju R, Li H, Zhu Z, Hu C, Qu J (2024). Synchronous in-situ sludge reduction and enhanced denitrification through improving electron transfer during endogenous metabolisms with Fe(II) addition. Water Research, 255: 121472

Langille M G I, Zaneveld J, Caporaso J G, McDonald D, Knights D, Reyes J A, Clemente J C, Burkepile D E, Vega Thurber R L, Knight R, Beiko R G, Huttenhower C (2013). Predictive functional profiling of microbial communities using 16S rRNA marker gene sequences. Nature Biotechnology, 31(9): 814−821

Li F, Wang X, Xu C (2023). Research progress on structural characteristics, structure-application relationships, and environmental application of biochar-supported zero valent iron (ZVI-BC). Current Pollution Reports, 9(2): 292−311

Liu Z, Cui Z, Guo Z, Li D, He Z, Liu W, Yue X, Zhou A (2024). Insights into the effect of nitrate photolysis on short-chain fatty acids production from waste activated sludge in anaerobic fermentation system: Performance and mechanisms. Water Research, 258: 121772

Lou T, Yin Y, Wang J (2024). Mechanisms of biochar promoting medium chain fatty acids production from sewage sludge: Effect of biochar type. Journal of Cleaner Production, 451: 141995

Qian L, Zhang W, Yan J, Han L, Chen Y, Ouyang D, Chen M (2017). Nanoscale zero-valent iron supported by biochars produced at different temperatures: Synthesis mechanism and effect on Cr(VI) removal. Environmental Pollution, 223: 153−160

Yin Y, Wang J (2016). Changes in microbial community during biohydrogen production using gamma irradiated sludge as inoculum. Bioresource Technology, 200: 217−222

Yin Y, Wang J (2021). Mechanisms of enhanced hydrogen production from sewage sludge by ferrous ion: Insights into functional genes and metabolic pathways. Bioresource Technology, 321: 124435

Yuan Y, Tao Y, Zhou S, Yuan T, Lu Q, He J (2012). Electron transfer capacity as a rapid and simple maturity index for compost. Bioresource Technology, 116: 428−434